

## Atomistic and multiscale analyses of brittle fracture in crystal lattices

Sulin Zhang,<sup>1,2,\*</sup> Ting Zhu,<sup>3</sup> and Ted Belytschko<sup>4</sup>

<sup>1</sup>Department of Mechanical Engineering, University of Arkansas, 204 Mechanical Building, Fayetteville, Arkansas 72701, USA

<sup>2</sup>Department of Engineering Science and Mechanics, The Pennsylvania State University, University Park, Pennsylvania 16802, USA

<sup>3</sup>Woodruff School of Mechanical Engineering, Georgia Institute of Technology, Atlanta, Georgia 30332, USA

<sup>4</sup>Department of Mechanical Engineering, Northwestern University, 2145 Sheridan Road, Evanston, Illinois 60201, USA

(Received 28 April 2007; revised manuscript received 17 July 2007; published 27 September 2007)

Applicability of the Griffith criterion [A. A. Griffith, *Philos. Trans. R. Soc. London, Ser. B* **221**, 163 (1920); S. Zhang, S. L. Meilke, R. Khare, D. Troya, R. S. Ruoff, G. C. Schatz, and T. Belytschko, *Phys. Rev. B* **71**, 115403 (2005)] for predicting the onset of crack extension in crystal lattices is systematically evaluated using atomistic and multiscale simulations with a focus on the effects of crack size and lattice discreteness. An atomistic scheme is developed to determine the true Griffith load defined by the thermodynamic energy balance of crack extension for both finite-sized and semi-infinite crack models. For a model monolayer lattice, we identify a characteristic crack length (about ten lattice spacings) below which the Griffith fracture stress markedly overestimates the true Griffith load. Through a stability analysis of crack-tip bond separation, the athermal (nonthermally activated) loads of instantaneous fracture are determined, thereby yielding the estimated lattice trapping range. Our simulations show that the strength of lattice trapping depends on the interaction range of the interatomic force fields. Using the reaction pathway exploration method, we determine the minimum energy paths of bond breaking and healing at a crack tip, giving a more precise estimate of the lattice trapping range. The activation energy barriers governing the rate of kinetic crack extension are extracted from the minimum energy paths. Implications concerning the distinction between the athermal and Griffith fracture loads are discussed. Based on these results, a general criterion is established to predict the onset of crack growth in crystal lattices. In addition to taking into account the lattice trapping effect, this criterion is applicable to a large spectrum of crack sizes.

DOI: 10.1103/PhysRevB.76.094114

PACS number(s): 61.72.-y, 61.50.Ah, 62.20.-x, 68.65.-k

### I. INTRODUCTION

Predicting the failure strength of nanostructured materials often involves quantum mechanical calculations or atomistic models with empirical force fields. While these numerical methods have been useful to elucidate the failure mechanisms at the atomic level, their prohibitive computational cost becomes a major concern for specimens of realistic size. In contrast, the fracture criteria<sup>1,2</sup> established within the framework of continuum fracture mechanics have been widely used to predict the critical conditions for the onset of crack extension in continua. If such continuum-based fracture criteria were applicable to nanostructured materials, the aforementioned computational burden could often be avoided. Thus, it is both fundamentally and practically critical to evaluate the applicability of these fracture criteria to crystal lattices with the consideration of flaw size and lattice discreteness.

The fundamental fracture criterion for brittle continua is the energy-balance criterion by Griffith,<sup>1,3</sup> which holds when there is no generation or motion of dislocations or other dissipation mechanisms, such as void nucleation. The Griffith criterion states that a crack meets the critical growth condition when the net change in the total energy of the system  $\Delta E$  vanishes upon crack extension by an infinitesimal distance  $\Delta a$ :

$$\Delta E = (G - 2\gamma_s)\Delta a = 0, \quad (1)$$

where  $G$  is the elastic energy release rate and  $\gamma_s$  is the surface energy density which measures the fracture resistance of the material. For a model system with a central crack of

length  $2a$  embedded in an infinitely large, linear elastic medium, subject to remotely applied uniform tension, the energy-balance criterion yields a critical stress<sup>1</sup>

$$\sigma'_G = \sqrt{2Y\gamma_s/\pi a} \quad (2)$$

for plane-stress condition, where  $Y$  denotes Young's modulus. To distinguish the critical stress given by Eq. (2) from the true Griffith load given by the energy-balance criterion of Eq. (1), the critical stress determined by Eq. (2) is hereafter referred to as the Griffith fracture stress.

The Griffith fracture stress has been widely used to predict the onset of crack extension in continua, yet it suffers deficiencies when applied to specimens with nanosized cracks. For extremely short cracks ( $a \rightarrow 0$ ), the Griffith fracture stress may exceed the theoretical strength  $\sigma_{th}$  of the perfect lattice, which, of course, is nonphysical. In addressing this issue, Gao *et al.*<sup>4</sup> suggested that a characteristic crack length can be identified as  $a^* \propto Y\gamma_s/\sigma_{th}^2$ , below which the Griffith fracture stress overestimates the true fracture stress and the material becomes flaw insensitive. Pugno and Ruoff<sup>5</sup> developed a quantized fracture mechanics (QFM) theory, where the classical stress intensity factor is redefined by considering an infinitesimal crack extension at the crack tip. With a predetermined geometric parameter, the QFM theory predicts satisfactory results on the fracture strengths of nanostructured materials. Recently, Mattoni *et al.*<sup>6</sup> proposed a modified Griffith condition, where Young's modulus and surface energy density are taken to be strain dependent. Despite yielding an improved agreement between the predicted Griffith fracture stress and the failure load, these

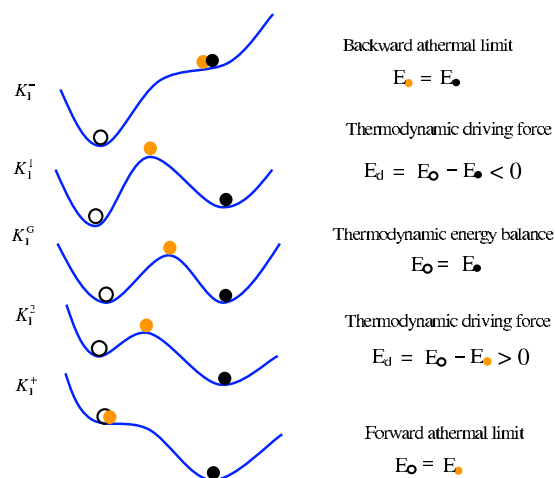


FIG. 1. (Color online) Load-mediated energy corrugation of a unit bond breaking and/or healing process at the crack tip. Within a range of applied load ( $K_I^- < K_I^1 < K_I^G < K_I^2 < K_I^+$ ), the crack tip can be stabilized at two local energy minima (denoted by an open circle and a black closed circle, respectively) separated by a saddle point (denoted by a yellow closed circle). At the Griffith load  $K_I^G$ , these two states are isoenergetic. Increasing the applied load from  $K_I^G$  causes the energy surface to tilt toward the second configuration (closed circle) with a reduced activation energy barrier (AEB) against bond breaking. A thermal limit  $K_I^+$  can be identified at which the AEB against bond breaking vanishes and bond breaking occurs without the aid of thermal activation. Similarly, decreasing the applied load from  $K_I^G$  causes the energy surface to tilt toward the first configuration (open circles) with a reduced AEB against bond healing. A thermal limit  $K_I^-$  can be identified at which the AEB against bond healing vanishes.

modifications were proposed without making connections to the energetics of brittle fracture on the atomic level.

From an atomic point of view, brittle crack extension in crystal lattices involves sequential bond breaking at the crack tip. A complete understanding of the fracture process at the nanoscale requires detailed atomic-level studies to elucidate the energetics governing this sequential bond-breaking process. Consider a straight crack in a two-dimensional (2D) lattice subject to mode I loading characterized by the stress intensity factor  $K_I$ , the energetics governing crack growth can be generically characterized by a load-mediated energy landscape of a unit bond-breaking process, as shown in Fig. 1. The final configuration (black closed circle) on the energy landscape differs from the initial one (open circle) in that the crack tip is advanced by one lattice spacing. These two configurations correspond to two local energy minima, and are separated by an energy barrier representing an intrinsic lattice resistance against bond breaking. The state with the highest energy is known as the saddle point (also as the transition state, yellow closed circle). The energy difference between the two local energy minima defines the thermodynamic driving force for crack-tip bond breaking (i.e., crack extension), while the energy difference between the saddle point and the first (second) local energy minimum gives rise to the activation energy barrier (AEB) governing the kinetic rate of bond breaking (healing). Starting from the Griffith

load  $K_I^G$  at which these two local energy minima are isoenergetic, with an increasing applied load, the energy landscape becomes tilted toward the final configuration with a reduced energy barrier against bond breaking. When the applied load reaches an athermal limit  $K_I^+$  at which the energy barrier vanishes,<sup>7</sup> the bond breaks spontaneously without the aid of thermal activation. Similarly, with a decreasing applied load, the energy landscape becomes tilted toward the first configuration, and an athermal limit  $K_I^-$  can be identified at which the bond heals spontaneously. At the Griffith load  $K_I^G$ , a finite lattice-resistance barrier exists between the isoenergetic states, which could trap the crack tip at either state, manifesting the lattice trapping effect.<sup>8</sup> The lattice trapping strength is defined by  $S \equiv (K_I^+ - K_I^-)/K_I^G$ , which characterizes the differences between the athermal limits in terms of the Griffith load for crack extension and healing.

The lattice-trapping effect may also be viewed as the consequence of the nonlinearity of the surface energy as the crack extends by less than one lattice spacing.<sup>8</sup> In contrast, continuum fracture mechanics assumes that the surface energy increases linearly with crack length, and is, thus, blinded to this nonlinear variation within one lattice spacing. Atomistic simulations<sup>9–20</sup> have been used to quantify the lattice-trapping strengths for different materials. A general conclusion from these studies is that lattice-trapping strength depends on the characteristics of the interatomic potentials, particularly the interaction range. By considering the forces exerted on the first several atomic bonds at the crack tip, Curtin<sup>21</sup> derived an analytical formula for the lattice-trapping strength in terms of the lattice properties and the characteristics of the empirical interatomic potentials.

In this paper, we systematically evaluate the applicability of the Griffith criterion for predicting the onset of crack extension in crystal lattices. Using a monolayer crystal lattice with a preexisting crack as a model system, the true Griffith load is determined by numerically identifying the load at which the energy-balance criterion of Eq. (1) is met for the unit advancement of a crack by one lattice spacing. We identify a characteristic crack size below which the Griffith fracture stress calculated by Eq. (2) markedly overestimates the true Griffith load. In addition to the athermal loads, the lattice-trapping strengths are determined for different empirical force fields. Using reaction pathway calculations,<sup>22–24</sup> we compute the load-mediated minimum-energy paths (MEPs) for the unit processes of crack-tip bond separation, thereby yielding the load-mediated AEBs against crack-tip bond breaking and healing.

The rest of the paper is organized as follows: Section II presents the numerical models and methodologies adopted in the simulations. Section III reports atomistic determinations of the true Griffith load and the lattice-trapping strength for the given empirical force fields. The load-mediated MEPs of the unit bond-breaking process computed by the nudged elastic band (NEB) method are also reported along with the corresponding AEBs. Discussions and concluding remarks are given in Secs. IV and V, respectively.

## II. MODELS AND METHODOLOGIES

### A. Models

A hexagonal monolayer crystal lattice containing either a finite-sized crack or a semi-infinite crack is adopted as our

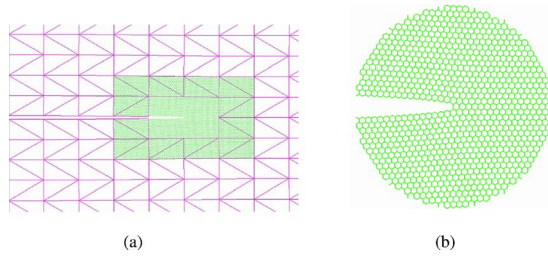


FIG. 2. (Color online) Monolayer lattice models. (a) The multi-scale model of a finite-size crack embedded in an infinite medium. Due to the configurational and loading symmetries, only half of the geometry is considered with an appropriately imposed symmetry condition. The crack tip is encompassed by an atomistic region, which is, in turn, embedded in a continuum domain discretized by finite elements. The continuum domain is only partially shown in the figure. (b) The model of a semi-infinite crack embedded in the local  $K$  field. Atoms at the outer boundary are held fixed, while all the other atoms are set free.

simulation model, as shown in Fig. 2. Such 2D hexagonal lattices are, for example, found in graphene sheets and, in curved form, carbon nanotubes. The finite-sized model [see Fig. 2(a)] is utilized to mimic the model system of a central crack embedded in an infinite elastic domain, where the overall dimensions of the lattice must at least be one order of magnitude larger than the crack length. For long cracks, atomistic simulations become computationally prohibitive. In such cases, a multiscale method coupling atomistics and finite elements is adopted. A detailed description of this coupling method can be found elsewhere.<sup>3,25,26</sup> Displacement boundary conditions are imposed on the edges of the lattice to simulate mode I crack extension. The configurational and loading symmetries allow us to use twofold symmetry in the simulations. The limited memory Broyden-Fletcher-Goldfarb-Shanno (BFGS) geometry optimization algorithm<sup>27</sup> is used to determine the minimum-energy configurations of the coupled and all-atom models. The stress state of the monolayer lattice is obtained by summing all forces acting on the edges divided by the edge length. Note that for the 2D monolayer lattice, stress and Young's modulus have the units of surface tension rather than pressure.

To model long cracks that extend self-similarly, a size-reduced model consisting of a small circular-shaped domain cut from the crack tip is adopted [see Fig. 2(b)]. The domain size is chosen such that its outer boundary falls in the  $K$ -dominant zone. The relatively small domain size makes all-atom simulations computationally feasible. Mode I loading is imposed by initially assigning all the atoms the displacement field given by the crack-tip asymptotic solution with a specified  $K_I^{\text{app}}$ . Atoms close to the outer boundary are held fixed, and the BFGS algorithm is employed to relax the atomic geometry, thereby obtaining the local energy-minimum configurations at applied loads.

### B. Empirical force fields and hyperelasticity

The fracture mechanisms of the monolayer lattice are fundamentally governed by the characteristics of the interatomic

force field. For the fracture of a monolayer graphene sheet, the second-generation Tersoff-Brenner (TB-G2) potential<sup>28</sup> has often been adopted to describe C-C covalent bonding, which takes the following form:

$$E = \sum_i \sum_{j>i} f_c(r_{ij}) [V^R(r_{ij}) + b_{ij}V^A(r_{ij})], \quad (3)$$

where  $E$  is the total energy of the atomic system,  $r_{ij}$  is the distance between atoms  $i$  and  $j$ ,  $V^R$  and  $V^A$  are the pairwise repulsive and attractive interactions, respectively,  $b_{ij}$  is a bond-order function (which has a complicated dependence on the bond angles and bond lengths involving atoms  $i$  and  $j$ ), and  $f_c$  is a cutoff function that reduces to zero for interactions beyond 2.0 Å. It should be noted that the TB-G2 potential leads to a spurious force-separation relation in that the interaction force is artificially raised for bond length between 1.7 and 2.0 Å due to the functional form of the cutoff function in the potential.<sup>29</sup> For the failure analysis of carbon nanotubes or graphene sheets,<sup>3,30</sup> a modified TB-G2 potential, denoted by MTB-G2,<sup>31</sup> has frequently been adopted, where the cutoff function is removed but includes C-C interactions only for those atom pairs that are less than 2.0 Å apart in the initial, undeformed configurations. The pair table is not updated throughout the simulation.

To study the influence of the interaction range of potentials on lattice-trapping strength, we also use a potential based on the many-body formalism of the MM2/MM3 model:

$$E = \sum_{\text{bonds}} V_s(r_{ij}) + \sum_{\text{angles}} V_\theta(\theta_{jik}, r_{ij}, r_{ik}). \quad (4)$$

The pair-body potential in the expansion is characterized by two matched quadratic functions:

$$V_s(r) = \begin{cases} \frac{1}{2}k_a(r-r_0)^2 - \gamma & (r < r_c) \\ \frac{1}{2}k_d(r-r_f)^2 & (r_c < r < r_f) \\ 0 & (r > r_f). \end{cases} \quad (5)$$

The parameters in the quadratic functions are chosen so that the potential is piecewise continuous and differentiable. The interatomic force for this potential is then bilinear. In the potential,  $r$  is the stretched bond length;  $r_0 = 1.42$  Å is the equilibrium bond length;  $r_c$  and  $r_f$  are the critical bond lengths at which bond force peaks and vanishes, respectively;  $k_a$  and  $k_d$  characterize, respectively, the ascending and descending slopes of the bilinear force-separation curve; and  $\gamma$  is the potential energy stored in the bond at equilibrium bond length, which is also equal to the area underneath the force-separation curve. The surface energy density is then  $\gamma_s = \gamma/2d_0$ , where  $d_0 = \sqrt{3}r_0$  is the lattice spacing. The three-body potential is a harmonic angle-bending energy term:

$$V_\theta = \frac{1}{2}k_\theta(\theta - \theta_0)^2, \quad (6)$$

where  $\theta_0 = 120^\circ$  is the equilibrium angle and  $k_\theta$  characterizes the angle-bending stiffness.

To facilitate the study of the lattice-trapping effect, four sets of parameters for the MM2/MM3 potential are adopted, where  $r_f$  (hence the descending slope  $k_d$  and the bond energy

$\gamma$ ) varies, while all the other parameters are the same ( $r_c = 1.524 \text{ \AA}$ ,  $k_a = 69.3 \text{ nN/\AA}$ , and  $k_\theta = 5.684 \text{ nN}$ ). These four potentials are denoted by I, II, III, and IV, respectively. Note that  $k_a$  and  $k_\theta$  uniquely determine Young's modulus and Poisson's ratio of monolayer lattices. Their values are chosen such that the resulting Young's moduli given by these potentials are comparable to that of a graphene sheet modeled by the Tersoff-Brenner potential.

The interaction range of a potential, characterized by a dimensionless parameter  $\beta \equiv (r_f - r_0)/(r_c - r_0)$ , determines the lattice-trapping strength. It was pointed out<sup>21</sup> that for  $\beta < \beta_0$ , the interaction range of the potential is short, while for  $\beta > \beta_0$ , the interaction range of the potential is long, where  $\beta_0$  is a constant depending only on the types of the crystal lattice but not on the potential, and can be determined by  $\beta_0 = 2\gamma/k_a\delta_G^2$ , where  $\delta_G$  is the elongation of the crack-tip bond at the true Griffith load. For triangular lattices  $\beta_0 = 3.68$ , and for hexagonal lattice  $\beta_0 = 7.85$ . Here,  $\beta$  is chosen to be 1.0, 2.5, 4.0, and 8.0, respectively, for these four MM2/MM3 potentials. Hence, the first three potentials are of short range, while the fourth one is of long range. Correspondingly, the parameter  $r_f$  for the four potentials is  $r_f^I = 1.524 \text{ \AA}$ ,  $r_f^{II} = 1.679 \text{ \AA}$ ,  $r_f^{III} = 1.835 \text{ \AA}$ , and  $r_f^{IV} = 2.249 \text{ \AA}$ , respectively, and the bond energy is  $\gamma^I = 0.233 \text{ eV}$ ,  $\gamma^{II} = 0.581 \text{ eV}$ ,  $\gamma^{III} = 0.931 \text{ eV}$ , and  $\gamma^{IV} = 1.862 \text{ eV}$ , respectively. For TB-G2,  $r_f$  coincides with the value of the cutoff in the cutoff function ( $r_f^{\text{TB-G2}} = 2.0 \text{ \AA}$ ), and it is a short-range potential since  $\beta = 1.46$ , while for MTB-G2,  $r_f^{\text{MTB-G2}} = \infty$  and, hence, is a long-range potential. The bond energy is 5.120 eV for TB-G2 and 4.908 eV for MTB-G2.

It should be noted that these MM2/MM3 potentials have zero out-of-plane bending rigidity, which is nonphysical. However, this is not of concern since in the present study crack extension is confined within the plane of the monolayer. These simple MM2/MM3 potentials do not accurately represent any real materials, but they present clear advantages in studying the effects of interatomic potentials on the energetics of brittle fracture.

The macroscopic material constants resulting from these potentials can be derived via the standard Cauchy-Born rule<sup>32</sup> following a lengthy but otherwise straightforward procedure.<sup>33,34</sup> The derived Young's modulus  $Y$  and Poisson's ratio  $\nu$  are 24.30 nN/ $\text{\AA}$  and 0.397, respectively, for the TB-G2 and MTB-G2 potentials, and 28.03 nN/ $\text{\AA}$  and 0.299, respectively, for the MM2/MM3 potentials. It should be noted that the hexagonal lattice is isotropic at infinitesimal deformation, but anisotropic at finite deformation.<sup>3,35</sup> Unless otherwise mentioned, Young's modulus and Poisson's ratio are referred to as the values at infinitesimal deformation.

### C. Minimum-energy paths of bond breaking and healing

A full understanding of the energetics governing crack growth or healing in brittle fracture entails probing the load-mediated energy landscape at the atomic level, as shown in Fig. 1. We apply the NEB method<sup>22-24</sup> to find the MEPs and calculate the associated AEBs for the unit process of bond breaking at a crack tip. The original NEB method has been

generalized to study a wide range of mechanics problems involving thermally activated processes, such as collapse of carbon nanotubes,<sup>36</sup> crack-tip dislocation nucleation,<sup>17</sup> slip transmission at the interface,<sup>37</sup> etc.

Prior to the NEB calculation, two local energy minima need to be identified, which correspond to the atomic equilibrium configurations before and after the breaking of the first bond at the crack tip. Thus, these two configurations can be considered as two distinct states along the fracture path. Taking the two configurations as fixed end states, an elastic band is constructed between them through a linear interpolation to create several equally spaced intermediate configurations (replicas). Nudged relaxation of the elastic band via the projected velocity Verlet method yields a discrete MEP. For the 2D atomic monolayer, the MEP is a continuous path in a  $2N$  dimensional configuration space (where  $N$  is the number of free atoms) along which the atomic forces are zero at any point in the  $2N-1$  dimensional hyperplane perpendicular to the path.<sup>38</sup> The calculations are considered converged when the force on each replica perpendicular to the path is less than 0.005 eV/ $\text{\AA}$ . A continuous MEP is generated by polynomial fitting of the discrete MEP.<sup>22</sup> AEBs against local bond breaking and bond healing can be extracted from the saddle points (the energy maximum along the path) on the MEPs. The applied loads at which the AEBs vanish are identified as the athermal loads for bond breaking or bond healing. It is understood that the lattice-trapping effect is caused by lattice discreteness and is independent of crack length. Thus, the semi-infinite crack model can be effectively used for the NEB calculation, though the NEB method is also applicable to the finite-sized crack model. In the NEB calculations, the  $K$ -field load is imposed by the displacement-control method, where boundary atoms are positioned according to the  $K$ -field displacement. To obtain a valid MEP, one needs to ensure that the positions of the boundary atoms are the same for all the replicas along the elastic band.

## III. RESULTS

### A. True Griffith loads

For very short cracks of length on the order of several lattice spacings, the Griffith fracture stress given by Eq. (2) may significantly deviate from the true Griffith load determined by the Griffith energy-balance criterion of Eq. (1). Computationally, the true Griffith load, denoted as  $\sigma_G$ , can be determined by finding the critical stress at which the net change of the total energy of the system vanishes upon unit crack extension by one lattice spacing,

$$\Delta E(\sigma_G) = E(a; \sigma_G) - E(a + d_0; \sigma_G) = 0, \quad (7)$$

where  $E(a; \sigma_G)$  and  $E(a + d_0; \sigma_G)$  denote the total energy of the system at the true Griffith load  $\sigma_G$  for crack lengths  $a$  and  $a + d_0$ , respectively.

#### 1. Finite-sized crack model

To determine the true Griffith load for a finite-sized crack as shown in Fig. 2(a), we consider two configurations with the crack lengths  $2a$  (denoted as configuration A) and  $2a$

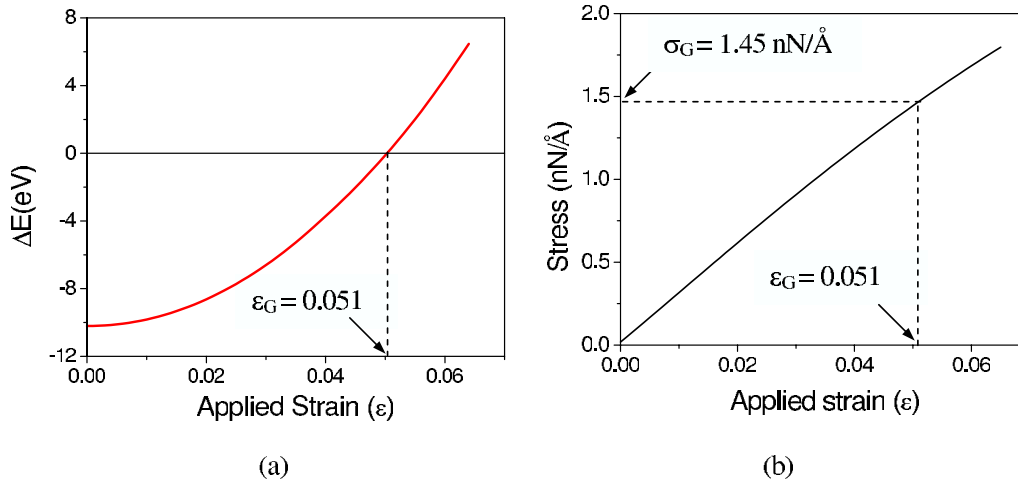


FIG. 3. (Color online) Atomistic determination of the true Griffith load for the finite-sized crack model ( $2a=10d_0$ ). TB-G2 is used in the simulations. (a) The difference in the total energy  $\Delta E$  between configurations A and B as a function of the applied strain  $\varepsilon$ . The Griffith strain  $\varepsilon_G$  is identified at which  $\Delta E$  vanishes. (b) The stress-strain curve for configuration A. The critical stress corresponding to the Griffith strain is identified as the true Griffith load  $\sigma_G$ .

$+2d_0$  (denoted as configuration B), respectively. These two configurations can be regarded as two consecutive states along the fracture path. The two configurations are stretched to fracture under displacement-controlled loading, yielding an energy-strain curve and a stress-strain curve. The total energy of each system is the sum of the elastic strain energy and surface energy. At the stress-free state, the difference in the total energy of these two configurations is solely due to their different surface energies. Under the same applied load, the strain energies of the two systems differ due to their different crack lengths and, thus, their different effective stiffness. However, this difference in strain energy will change with increasing load; at a critical applied stress, it compensates with the difference in surface energy, and the total energies of the two configurations become the same; namely, configurations A and B are two isoenergetic states along the fracture path under the same applied load. By definition, this critical applied stress corresponds to the true Griffith load  $\sigma_G$ .

A series of calculations were performed with crack lengths  $2d_0 < a < 100d_0$  to determine the true Griffith load for TB-G2. Cracks were created by removing a row of atomic bonds, although this is not a chemically realistic model for a crack.<sup>39</sup> A more appropriate model for a crack is obtained by removing a row of atoms.<sup>3,30</sup> Since the present focus is on the mechanical aspects of the system and we are considering longer cracks, the chemical constraint is temporarily not taken into account for numerical convenience. To model the extension of a central crack embedded in an infinite medium, the dimensions of the simulation model should be sufficiently large to suppress the boundary effects. Thus, for crack length greater than 20 lattice spacings, the coupling method<sup>3,25</sup> is adopted to reduce the computational cost. Figure 3 illustrates the search for the true Griffith load for a crack with length of  $10d_0$  using the TB-G2 potential. At zero strain (stress-free state), the energy difference of these two states  $\Delta E \equiv E_A - E_B$  is finite and solely due to the surface energy difference. With an increasing applied strain  $\varepsilon$ , the

magnitude of the energy difference of the two states monotonically decreases [Fig. 3(a)]. The strain at which the energy difference vanishes is identified as the Griffith strain, denoted by  $\varepsilon_G$ , and the corresponding applied load in the stress-strain curve is the true Griffith load  $\sigma_G$  [Fig. 3(b)]. Beyond the true Griffith load, the difference in the strain energies stored in these two stretched configurations exceeds the difference in the surface energies, and  $\Delta E$  continues increasing until fracture occurs.

## 2. Semi-infinite crack model

For the semi-infinite crack model depicted in Fig. 2(b), the true Griffith load for mode I fracture can also be determined based on the energy-balance criterion of Eq. (7). At a given  $K_I^{\text{app}}$ , all the atoms in the system are initially positioned according to the displacement field of the crack-tip asymptotic solution:

$$\begin{Bmatrix} u_x \\ u_y \end{Bmatrix} = \frac{K_I^{\text{app}}}{2\mu} \sqrt{\frac{r}{2\pi}} (\kappa - \cos \theta) \begin{Bmatrix} \cos(\theta/2) \\ \sin(\theta/2) \end{Bmatrix}, \quad (8)$$

where  $r$  and  $\theta$  are defined with the origin  $O$  at the center of the first bond at the crack tip (see Fig. 4),  $\mu$  is the shear modulus of the lattice, and  $\kappa = (3-\nu)/(1+\nu)$ . Atoms about  $3 \text{ \AA}$  from the outer boundary are held fixed, while the remainder of atoms are relaxed using the BFGS algorithm, thereby yielding an optimized configuration A with a minimized total system energy  $E_A$ . Note that configuration B can be regarded as a replica of A at the same applied load, but with the first bond at the crack tip broken. To search for configuration B using geometry optimization, one needs to make an initial guess that is sufficiently close to the local energy minimum corresponding to configuration B. Otherwise, the BFGS search would converge to configuration A. While there are several schemes that can be used to obtain an initial guess sufficiently close to configuration B, the following algorithm is found most effective, and thus used in our simulations. With the same starting configuration, all atoms

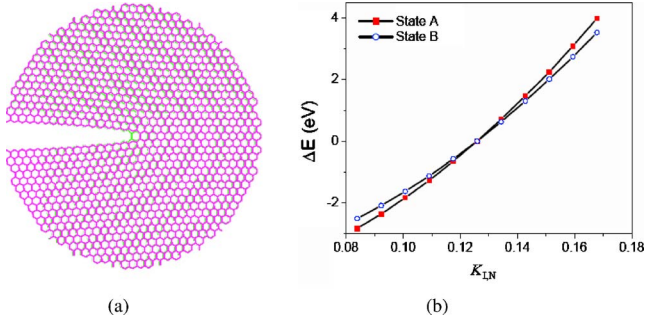


FIG. 4. (Color online) Atomistic determination of the true Griffith load for potential II using the semi-infinite crack model. (a) The local energy-minimum configurations at the true Griffith load. These two configurations are overlapped; the green lattice stands for configuration A and the purple lattice for configuration B. Configuration B differs from A in that the bond at the crack tip is broken. (b) The relative energetics for configurations A and B as a function of the applied load. The energy at the Griffith load is taken as the reference. The red squares represent the energy state A, while the blue circles represent the energy state B. The intersection of these two curves identifies the true Griffith load. For a load less than the Griffith load, state A is energetically favored, while for a load larger than the Griffith load, state B is energetically favored.

are positioned according to the displacement field described by Eq. (8), but with a reference origin  $O'$  that is located one lattice spacing ahead of the origin  $O$ . The free atoms in the system are then relaxed, yielding an intermediate optimized configuration  $B'$  with a total free system energy  $E_{B'}$ . By using the new origin  $O'$ , the local opening displacement imposed on the first bond at the crack tip is much larger than that if the origin  $O$  were otherwise used. As a result, the first bond in configuration  $B'$  is broken within a certain range of applied  $K_I^{\text{app}}$ . Note that configurations A and  $B'$  are subjected to different boundary conditions since the applied displacements on the boundary atoms are based on different origins, even though the magnitudes of  $K_I^{\text{app}}$  are the same for both cases. We then change the positions of the fixed atoms at the boundary of configuration  $B'$  according to the asymptotic displacement field with the reference origin  $O$ , yet do not reposition the free atoms in the system. Further relaxation of the system  $B'$  under the newly imposed boundary condition gives rise to a relaxed configuration B with a total energy  $E_B$ . This scheme effectively traps the crack tip at the second energy minimum, i.e., configuration B, for a range of applied load except for MTB-G2. Figure 4(a) shows an example of the (overlapped) lattice structures of configurations A and B at a certain applied load.

Without updating the pair table in the simulations using MTB-G2 (reflecting its infinite interaction range), we had difficulties finding configuration B. To resolve this difficulty, the pair table for MTB-G2 is updated with a sufficiently large cutoff radius so that the modified potential is still of long range, i.e.,  $\beta > \beta_0$ . This treatment introduces negligible changes to the bond energy of MTB-G2. Therefore, the energetics closely approximates that of MTB-G2.

A comparison between  $E_A$  and  $E_B$  suggests the relative stability of configurations A and B. If  $E_A < E_B$ , it indicates

TABLE I. Comparisons between the true Griffith load  $\sigma_G$ , the Griffith fracture stress  $\sigma'_G$ , and the fracture load (athermal load)  $\sigma_f$  for the TB-G2 potential. For cracks of length longer than  $10d_0$ , the difference of  $\sigma_G$  and  $\sigma'_G$  becomes insignificant. The ratio  $\sigma_f/\sigma_G$  is nearly constant, indicating that lattice-trapping effect is independent of crack length. In the table, the crack length has a unit of lattice spacing, while the stress has a unit of  $\text{nN}/\text{\AA}$ .

Crack length	$\sigma_G$	$\sigma'_G$	$\sigma_f$	$\sigma_f/\sigma_G$
4	2.13	2.60	2.79	1.31
6	1.79	2.01	2.37	1.32
8	1.60	1.70	2.09	1.31
10	1.45	1.50	1.92	1.32
12	1.34	1.36	1.78	1.33
14	1.25	1.26	1.65	1.32
16	1.16	1.18	1.54	1.33
50	0.64	0.67	0.84	1.31
100	0.45	0.46	0.59	1.31
200	0.32	0.33	0.42	1.31

that under the applied load  $K_I^{\text{app}}$  configuration A is energetically favored, and hence, the applied load is less than the Griffith load, i.e.,  $K_I^{\text{app}} < K_I^G$ ; on the other hand, if  $E_A > E_B$ , configuration B is energetically favored and  $K_I^{\text{app}} > K_I^G$ . Adjusting the applied load eventually leads to the Griffith load such that  $E_A = E_B$ . To reduce the search range, one can first estimate an approximate Griffith load, and then perform the numerical search. Specifically, using the relationship between the critical stress intensity factor  $K_{\text{th}}^G$  and the energy release rate  $G_I = (K_{\text{th}}^G)^2/Y$  for linear elastic materials, and note that the critical energy release rate is twice of the surface energy density  $\gamma_s$ , one has

$$K_{\text{th}}^G = \sqrt{2Y\gamma_s}. \quad (9)$$

Figure 4(b) shows the relative energetics of the two configurations for potential II, where the horizontal axis  $K_{I,N}$  is the applied  $K$  load normalized by  $2\mu\sqrt{r_0}$ . From hereafter, the subscript  $N$  means normalized value unless otherwise mentioned. The system energy at the true Griffith load is used as the reference energy for the energy of states at other applied loads. The applied load at which the two curves intersect is identified as the normalized Griffith load  $K_{G,N}$ .

## B. Crack-size effect

Table I lists the true Griffith load  $\sigma_G$  determined by Eq. (7) and the Griffith fracture stress  $\sigma'_G$  from Eq. (2) for the TB-G2 potential. We found that  $\sigma'_G$  is markedly larger than  $\sigma_G$  for crack size less than  $10d_0$ . As the crack size increases, the difference in these two loads becomes negligibly small. Such small difference may be partially due to either the computational precision, the anisotropy of the lattice at finite strain, or the nonlinearity of the material. The coupling between the atomistics and the finite element scheme may also account for some of the difference. The observed crack-size effect arises from crack geometry, and should be independent

TABLE II. The atomistically determined true Griffith load  $K_{G,N}$ , the theoretical Griffith load  $K'_{G,N}$  predicted by Eq. (9), and the critical loads  $K_{A,N}$  and  $K_{B,N}$  at which configurational instability occurs. All the loads are normalized by  $2\mu\sqrt{r_0}$ . For each of the four MM2/MM3 potentials, the values for  $K_{G,N}$  and  $K'_{G,N}$  are the same, while for TB-G2 and MTB-G2, the difference of these two values is about 1% due to nonlinearity. For the short-range MM2/MM3 potentials ( $\beta < \beta_0 = 7.85$ ), the values of  $K_{A,N}$  are the same, while the values of  $K_{B,N}$  are approximately proportional to the bond energy  $\gamma$  (unit: eV). Lattice-trapping strengths  $S$  approximated by  $(K_{A,N} - K_{B,N})/K_{G,N}$  for these MM2/MM3 potentials monotonically decrease with increasing interaction range of the potentials. For long-range potentials (IV and MTB-G2), the differences in three loads,  $K_{B,N}$ ,  $K_{G,N}$ , and  $K_{A,N}$  are negligibly small.

Potentials	$\beta$	$\gamma$	$K'_{G,N}$	$K_{G,N}$	$K_{A,N}$	$K_{B,N}$	$\gamma/K_{B,N}$	$S$
I	1.0	0.233	0.080	0.080	0.219	0.029	8.17	2.39
II	2.5	0.581	0.126	0.126	0.219	0.071	8.15	1.18
III	4.0	0.931	0.162	0.162	0.219	0.115	8.10	0.65
IV	8.0	1.862	0.229	0.229	0.232	0.227	8.20	0.02
TB-G2	1.46	5.120	0.434	0.429	0.571	0.225	21.92	0.81
MTB-G2	$\infty$	4.908	0.425	0.422	0.426	0.420	11.68	0.01

of interatomic potentials, as verified by our studies using other potentials. Hence, we conclude that the characteristic length  $a^* \sim 10d_0$  below which the Griffith fracture stress given by Eq. (2) becomes inaccurate is generally valid to *any* elastic crystal.

Table I also lists the fracture strengths  $\sigma_f$ , defined as the critical stress of fracture initiation in the energy minimization of the system at a prescribed load, as detailed in the succeeding section. Evidently, the fracture strengths are much larger than the corresponding Griffith loads, suggesting appreciable lattice-trapping effects, which will also be discussed in the succeeding section. We note that the ratio  $\sigma_f/\sigma_G$  is almost constant for all the potentials ( $\sim 1.3$  for TB-G2 as shown in Table I, for example) and the range of the crack length considered, which indicates that the lattice-trapping strength is independent of crack length.

In Table II, we list the true Griffith loads for all the potentials considered, along with the theoretically predicted Griffith loads based on Eq. (9). For different potentials, the true Griffith load is fairly close to the theoretical predictions, indicating that nonlinearity plays a negligible role on the Griffith load. We also note that the true Griffith load determined for the semi-infinite crack model is consistent with that for the finite-sized model. This consistency can be seen from the relation  $K_G \cong \sigma_G \sqrt{\pi a}$  for long cracks.

### C. Lattice-trapping effect

The athermal limits can be approximately determined by the stability analysis of crack-tip bond separation. Since the lattice-trapping strength is independent of crack size, the semi-infinite crack model can be effectively utilized for such calculations. From the true Griffith load, we increase the applied load incrementally and perform energy minimization at each load. We find that at a critical load  $K_A$ , which is above  $K_G$ , configuration A can no longer be stabilized, manifested by the fact that the BFGS relaxation yields configuration B. Similarly, a critical load  $K_B$ , which is below  $K_G$ , can be found at which configuration B becomes unstable. Note that

$K_A$  always underestimates the true athermal load  $K^+$ , and  $K_B$  always overestimates  $K^-$ . This can be understood as follows. When the applied load is fairly close to the athermal limits  $K^+$  (or  $K^-$ ), the energy well trapping configuration A (or B) is so shallow that the AEB is very small. Thus, in the course of relaxing an initially guessed state A (or B), the shallow energy well may not be able to trap the crack tip, and the system would then relax to state B (or A). As a result, using this algorithm, the lattice trapping strength determined by  $(K_A - K_B)/K_G$  is a lower limit of  $(K^+ - K^-)/K_G$ .

The calculated  $K_A$  and  $K_B$  are listed in Table II along with the lattice-trapping strength. Of particular note is the effect of potentials. For the MM2/MM3 potentials, our simulations show that the lattice-trapping strength monotonically decreases with increasing interaction range of the potential and becomes negligibly small for long-range potentials. This observation agrees with the previous studies.<sup>9,10,21</sup> Specifically, for the three short-range MM2/MM3 potentials (I, II, and III), the athermal limits  $K_A$  governing bond breaking are the same, while the athermal limit  $K_B$  governing bond healing monotonically increases with increasing interaction range of the potentials. The athermal limit  $K_A$  for potential IV is about 5% larger than that for the other three MM2/MM3 potentials. These observations can be understood based on crack-tip bond instability. In general, the crack-tip bonds are subject to an extension force exerted by the surrounding lattice. The bonds themselves also yield a restoring force at a given bond length. Occurrence of bond instability is a result of the competition between these two forces. For short-range potentials, the ‘‘one-atom core’’ assumption of Thomson *et al.*<sup>40</sup> holds, under which the bond behind the crack tip yields a vanishing restoring force when the restoring force of the crack-tip bond reaches its peak,  $f_p$ . Under this condition, the crack-tip bond becomes locally unstable to an infinitesimal extension when the stretching force exerted to the crack-tip bond by the surrounding lattice reaches the peak force. Since the peak forces for the three short-range MM2/MM3 potentials are all the same, therefore the athermal limits  $K_A$  are all the same. For long-range potentials, however, the bond behind the crack tip also supplies some additional restoring force when the first

bond at the crack tip reaches its peak. Thus, the stretching force corresponding to local bond instability, i.e., the athermal limit  $K_A$ , is slightly larger. Oppositely, the crack-tip bond becomes locally unstable to an infinitesimal contraction (healing) when the applied load reaches a point at which the restoring force is larger than the extension force. This applied load  $K_B$  depends on the slope of the descending portion of the potential. For the current setting, since the peak forces of the MM2/MM3 potentials are all the same,  $K_B$  appears to be proportional to the bond energy, manifested by the fact that  $\gamma/K_B$  is almost a constant for the three short-range MM2/MM3 potentials, as seen in Table II. For the long-range MM2/MM3 potential, because the bond next to the crack tip also supplies some restoring force, the value  $\gamma/K_B$  for potential IV is slightly larger than those for the other MM2/MM3 potentials. A quantitative analysis of the restoring forces of the bonds near the crack tip was given by Curtin.<sup>21</sup>

The athermal limits  $K_A$  calculated for TB-G2 and MTB-G2 further support that the peak force of the bond governs the athermal limit  $K_A$ . Since TB-G2 possesses a higher peak force than MTB-G2, thus,  $K_A$  for TB-G2 is larger than that for MTB-G2. Table II also shows that the true Griffith load always falls within  $K_A$  and  $K_B$ , i.e.,  $K_B < K_G < K_A$ . For the two long-range potentials, potential IV and MTB-G2, the difference between the athermal loads  $K_A$  and  $K_B$ , and the true Griffith load is negligibly small. This concludes that for long-range potentials, the true Griffith load is a fairly accurate approximation for the athermal limit governing bond breaking.

#### D. Load-mediated minimum-energy paths and activation energy barriers

Once the two local energy-minimum configurations A and B are identified at the same applied load  $K_I^{\text{app}}$ , a discrete MEP connecting the two local energy minima can be computed using the NEB method. In our NEB calculations, the elastic band consists of 18 equally spaced intermediate replicas that are linearly interpolated from the two end images, i.e., configurations A and B. Continuous MEPs are obtained by polynomial fitting based on the discrete MEP.<sup>22</sup> Since the relative energetics of the initial and final configurations on the elastic band is dependent on the applied load, the MEPs are also load dependent.

Using potential II as an example, Fig. 5 shows the MEPs at two different applied loads. Note that  $K_{I,N} = 0.126$  is the normalized true Griffith load for potential II. In the figure, the symbols denote the calculated energies of replicas along the MEPs, while the solid lines are the fitted curves. The energy of configuration A is used as a reference for other replicas. For replica  $i$ , the reaction coordinate  $s_i$  is defined as

$$s_i = l_i/l_N, \quad (10)$$

where  $l_i = \|\mathbf{x}_i - \mathbf{x}_1\|$  and  $l_N = \|\mathbf{x}_N - \mathbf{x}_1\|$  are the Euclidean distances between the intermediate replica  $i$  and the first image (configuration A), and between the  $N$ th replica (configuration B) and the first, respectively. Thus,  $s_i$  runs from 0 (for configuration A) to 1 (for configuration B). The energy differ-

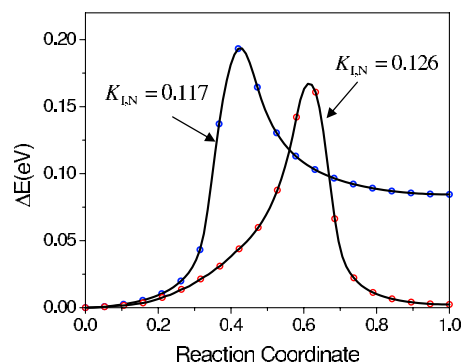


FIG. 5. (Color online)  $K$ -mediated minimum-energy paths of the unit process of crack-tip bond breaking for potential II.

ence between the saddle point state and configurations A or B defines the AEB. As expected, a higher applied load leads to a lower (higher) AEB against bond breaking (healing).

The quantification of AEBs allows us to determine the athermal limits more accurately as compared with stability analysis of crack-tip bond separation, as described in the previous section. With computed AEBs at a series of applied loads, a polynomial fitting and extrapolation of the barrier versus load relations yield the athermal limits at which the associated barriers vanish. As an example, Fig. 6 shows the extrapolated curves for potential II for both bond breaking and bond healing. The intersection of these two curves identifies the true Griffith load at which the barriers for bond breaking and bond healing are the same. It shows that close to the athermal limits, the energy barrier changes slightly with load. The continuous decrease in the slope of the barrier-load curve may be attributed to the elastic softening at large strains, and will lead to a significant underestimation (overestimation) of  $K_I^+$  ( $K_I^-$ ) if using a simple scheme of linear extrapolation. For potential II, the extrapolated data yield  $K_{I,N}^+ = 0.227$ , which is slightly larger than  $K_{A,N}$ , and  $K_{I,N}^- = 0.067$ , which is slightly smaller than  $K_{B,N}$ .

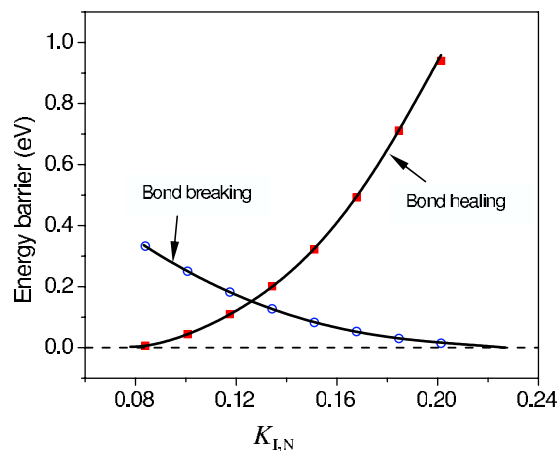


FIG. 6. (Color online) Activation energy barriers for bond breaking and bond healing as a function of the normalized applied  $K$  for potential II. The intersection of the two fitted curves identifies the energy barrier at the true Griffith load. Curve extrapolation identifies the athermal limits for bond breaking and healing at which the associated activation energy barriers vanish.

## IV. DISCUSSIONS

### A. Kinetic rate of crack extension

The calculated AEBs,  $\Delta E_{\text{act}}$ , can be utilized to estimate the kinetic rate of crack growth,

$$v = d_0 f_0 \exp \left[ - \frac{\Delta E_{\text{act}}(K)}{k_B T} \right], \quad (11)$$

where  $k_B$  is Boltzmann's constant,  $T$  is the temperature, and  $f_0$  is the attempt frequency, typically on the order of  $10^{13}/\text{s}$ . If the Griffith energy-balance criterion is taken as the critical condition of instantaneous crack extension, the underlying assumption is that the local energy corrugation, as measured by  $\Delta E_{\text{act}}$ , is sufficiently small so that the success rate of crack-tip bond breaking by thermal activation is high, thus giving large  $v$ . However, as shown in our simulations, the AEB could be very high depending on the characteristics of the interatomic potentials. Consequently, the athermal load could be much higher than the Griffith load. In such cases, the Griffith energy-balance criterion is not accurate for predicting the onset of instantaneous crack extension.

### B. Generalized fracture criterion

Our simulations have demonstrated that for long-range potentials, the lattice trapping effect is insignificant and the true Griffith load provides a fairly close estimate of the athermal limit. In contrast, for materials exhibiting significant lattice-trapping effect, the athermal limit governing local bond instability is a better approximation of the fracture load than the Griffith load. According to our numerical analysis, the athermal limit  $\sigma_A$  for bond breaking is proportional to the true Griffith load, thus

$$\sigma_A = \eta_0 \sigma_G \approx \alpha \frac{f_P}{\sqrt{d_0 a}}, \quad (12)$$

where  $\eta_0$  is a scaling factor reflecting the lattice trapping against bond breaking, and is approximately equal to 1.3 and 1.7, respectively, for TB-G2 and potential II. Note that for sufficiently long cracks, the athermal load governing bond breaking is proportional to the peak force of the potentials and inversely proportional to  $\sqrt{a}$ . Hence, the approximation in Eq. (12) holds since it is not accurate for short cracks (for short cracks, the athermal limit is not inversely proportional to  $\sqrt{a}$ ). Here,  $\alpha$  is a material constant depending on the lattice type and crystallographic orientation of the fracture path, and can be numerically determined. For TB-G2,  $\alpha \cong 1.46$ . Thus, a fracture criterion can be proposed to account for the crack-size and lattice-trapping effects simultaneously:

$$\sigma_f = \eta \sigma_G, \quad (13)$$

where

$$\eta = \begin{cases} 1, & \beta > \beta_0 \\ \eta_0, & \beta \leq \beta_0. \end{cases} \quad (14)$$

Note that for long cracks and materials characterized by long-range potentials, the Griffith fracture stress is a close

estimate of the true Griffith load as well as the athermal load for bond breaking. Thus, the Griffith formula is still a valid onset condition for predicting crack propagation under these conditions.

## V. CONCLUDING REMARKS

We have studied the applicability of the Griffith criterion for predicting fracture of crystal lattice via detailed atomistic and multiscale analyses of bond breaking and healing at the crack tip. We have developed computational schemes for atomistically determining the true Griffith load for both the finite-sized and semi-infinite crack models. For a model system of monolayer lattice, we found that below a characteristic crack size of about ten lattice spacings, the Griffith fracture stress markedly overestimates the true Griffith load because the energy release rate estimate provided by the continuum solution becomes inaccurate.

The stability analysis of crack-tip bond separation yields an estimate of the athermal loads  $K^+$  and  $K^-$  at which the crack tip becomes locally unstable to bond breaking and healing, respectively. We show that the critical load  $K^+$  governing bond breaking depends on the peak force of the bond, while  $K^-$  governing bond healing depends on the descending portion of the force-separation relations. The lattice-trapping strengths calculated for the MM2/MM3 potentials show a clear dependence on the interaction range of the potential: with increasing interaction range, the lattice-trapping strength decreases.

The local corrugation in the energy landscape of the cracked lattice causes the difference between the true Griffith load and the athermal load of instantaneous fracture, resulting in the lattice-trapping effect. Using the reaction pathway calculations, load-mediated minimum-energy paths were determined, and the activation energy barriers were calculated. Polynomial fitting and extrapolation of the barrier versus load curve provide a more accurate scheme for determining the lattice-trapping strength. The activation energy barriers can also be used to estimate the kinetic rate of crack extension.

A generalized fracture criterion accounting for both the lattice-trapping effect and crack-size effect is established by considering two typical regimes of interaction range of the potentials. For long-range interatomic potentials, lattice trapping of bond breaking at the crack tip is negligible and the true Griffith load is a fairly accurate onset condition for crack extension. We emphasize that the true Griffith load satisfies the thermodynamic energy balance, which is very different from the Griffith fracture stress estimated by Eq. (2) when the crack length is less than ten lattice spacings. For cracks longer than ten lattice spacings, the true Griffith load can be approximated by the Griffith fracture stress. Thus, the crack-size effect is naturally taken into account. In contrast, for short-range interaction potentials, the lattice-trapping effect is more significant, so that the athermal limit for bond breaking yields a more appropriate onset condition for instantaneous lattice fracture.

Besides providing important physical insights into brittle fracture of crystal lattices by cleavage bond ruptures, the

computational schemes developed in this work are general and can be applied to study the energetics and kinetics of ductile fracture involving dislocation nucleation or motion at a crack tip. Brittle fracture by bond breaking generally prevails at low temperatures. There exists a critical temperature at which ductile fracture by dislocation motions prevails and brittle-to-ductile transition occurs. A study of such phenomena in systems of flat monolayer lattices and curved monolayers of single-walled carbon nanotubes is currently under way.

## ACKNOWLEDGMENTS

S.Z. acknowledges the support from the National Science Foundation (NSF) Grant No. CMMI-0600661. T.Z. acknowledges the support from NSF Grant No. CMMI-0653769 and AFOSR/MURI Grant No. F49620-02-1-0382. T.B. acknowledges the support from NSF Grant No. CMMI-0304472 and from the NASA University Research, Engineering and Technology Institute on Bio Inspired Materials (BIMat) under Award No. NCC-1-02037.

\*Corresponding author; suz10@psu.edu

- <sup>1</sup>A. A. Griffith, *Philos. Trans. R. Soc. London, Ser. A* **221**, 163 (1920).
- <sup>2</sup>J. R. Rice, *J. Appl. Mech.* **35**, 379 (1968).
- <sup>3</sup>S. Zhang, S. L. Meilke, R. Khare, D. Troya, R. S. Ruoff, G. C. Schatz, and T. Belytschko, *Phys. Rev. B* **71**, 115403 (2005).
- <sup>4</sup>H. J. Gao, B. H. Ji, I. L. Jager, E. Arzt, and P. Fratzl, *Proc. Natl. Acad. Sci. U.S.A.* **100**, 5597 (2003).
- <sup>5</sup>N. M. Pugno and R. S. Ruoff, *Philos. Mag.* **84**, 2829 (2004).
- <sup>6</sup>A. Mattoni, L. Colombo, and F. Cleri, *Phys. Rev. Lett.* **95**, 115501 (2005).
- <sup>7</sup>A. S. Argon, *Scr. Metall.* **16**, 259 (1982).
- <sup>8</sup>R. Thomson, C. Hsieh, and V. Rana, *J. Appl. Phys.* **42**, 3154 (1971).
- <sup>9</sup>D. M. Esterling, *J. Appl. Phys.* **47**, 486 (1976).
- <sup>10</sup>P. Gumbsch and R. M. Cannon, *MRS Bull.* **25**, 15 (2000).
- <sup>11</sup>K. Kitamura, I. L. Maksimov, and K. Nishioka, *Philos. Mag. Lett.* **75**, 343 (1997).
- <sup>12</sup>T. Odagaki, *J. Phys. A* **20**, 6455 (1987).
- <sup>13</sup>A. Paskin, D. K. Som, and G. J. Dienes, *J. Phys. C* **14**, L171 (1981).
- <sup>14</sup>J. E. Sinclair, *Philos. Mag.* **31**, 647 (1975).
- <sup>15</sup>J. C. H. Spence, Y. M. Huang, and O. Sankey, *Acta Metall. Mater.* **41**, 2815 (1993).
- <sup>16</sup>T. Zhu, J. Li, and S. Yip, *Phys. Rev. Lett.* **93**, 205504 (2004).
- <sup>17</sup>T. Zhu, J. Li, and S. Yip, *Phys. Rev. Lett.* **93**, 025503 (2004).
- <sup>18</sup>T. Zhu, J. Li, and S. Yip, *Trans. ASME, J. Appl. Mech.* **72**, 932 (2005).
- <sup>19</sup>J. R. Rice, *J. Mech. Phys. Solids* **26**, 61 (1978).
- <sup>20</sup>T. Zhu, J. Li, and S. Yip, *Proc. R. Soc. London, Ser. A* **462**, 1741 (2006).
- <sup>21</sup>W. A. Curtin, *J. Mater. Res.* **5**, 1549 (1990).
- <sup>22</sup>G. Henkelman and H. Jonsson, *J. Chem. Phys.* **113**, 9978 (2000).
- <sup>23</sup>G. Henkelman, B. P. Uberuaga, and H. Jonsson, *J. Chem. Phys.* **113**, 9901 (2000).
- <sup>24</sup>H. Jonsson, G. Mills, and K. W. Jacobsen, in *Classical and Quantum Dynamics in Condensed Phase Simulations*, edited by B. J. Berne, G. Ciccotti, and D. F. Coker (World Scientific, Singapore, 1998), p. 385.
- <sup>25</sup>S. P. Xiao and T. Belytschko, *Comput. Methods Appl. Mech. Eng.* **193**, 1645 (2004).
- <sup>26</sup>S. Zhang, R. Khare, Q. Lu, and T. Belytschko, *Int. J. Numer. Methods Eng.* **70**, 913 (2007).
- <sup>27</sup>J. C. Gilbert and J. Nosedal, *Appl. Math. Lett.* **6**, 47 (1993).
- <sup>28</sup>D. W. Brenner, O. A. Shenderova, J. A. Harrison, S. J. Stuart, B. Ni, and S. B. Sinnott, *J. Phys.: Condens. Matter* **14**, 783 (2002).
- <sup>29</sup>T. Belytschko, S. P. Xiao, G. C. Schatz, and R. S. Ruoff, *Phys. Rev. B* **65**, 235430 (2002).
- <sup>30</sup>S. L. Mielke, D. Troya, S. Zhang, J. L. Li, S. P. Xiao, R. Car, R. S. Ruoff, G. C. Schatz, and T. Belytschko, *Chem. Phys. Lett.* **390**, 413 (2004).
- <sup>31</sup>O. A. Shenderova, D. W. Brenner, A. Omeltchenko, X. Su, and L. H. Yang, *Phys. Rev. B* **61**, 3877 (2000).
- <sup>32</sup>M. Born and M. Huang, *Dynamical Theory of Crystal Lattices* (Oxford University Press, Oxford, 1954).
- <sup>33</sup>M. Arroyo and T. Belytschko, *Int. J. Numer. Methods Eng.* **59**, 419 (2004).
- <sup>34</sup>T. C. Chang and H. J. Gao, *J. Mech. Phys. Solids* **51**, 1059 (2003).
- <sup>35</sup>D. Troya, S. L. Mielke, and G. C. Schatz, *Chem. Phys. Lett.* **382**, 133 (2003).
- <sup>36</sup>S. Zhang, R. Khare, T. Belytschko, K. J. Hsia, S. L. Mielke, and G. C. Schatz, *Phys. Rev. B* **73**, 075423 (2006).
- <sup>37</sup>T. Zhu, J. Li, A. Samanta, H. Kim, and S. Suresh, *Proc. Natl. Acad. Sci. U.S.A.* **104**, 3031 (2007).
- <sup>38</sup>M. R. Sorensen, Y. Mishin, and A. F. Voter, *Phys. Rev. B* **62**, 3658 (2000).
- <sup>39</sup>R. Khare, S. L. Mielke, J. T. Paci, S. Zhang, R. Ballarini, G. C. Schatz, and T. Belytschko, *Phys. Rev. B* **75**, 075412 (2007).
- <sup>40</sup>R. Thomson, V. K. Tewary, and K. Masuda-Jindo, *J. Mater. Res.* **2**, 619 (1987).